Monatsh Chem (2011) 142:1087–1095
DOI 10.1007/s00706-011-0622-3

ORIGINAL PAPER

New rare earth-rich aluminides and indides with cubic Gd_4RhIn-type structure

Frank Tappe · Christian Schwickert · Stefan Linsinger · Rainer Pöttgen

Received: 4 July 2011 / Accepted: 5 August 2011 / Published online: 16 September 2011

Abstract The series of rare earth metal (*RE*)-rich intermetallics RE_4TAl and RE_4TIn (T = Ru, Rh, Ir) were synthesized by induction melting of the elements in sealed tantalum tubes. These compounds crystallize with the cubic Gd_4RhIn-type structure, space group $F\bar{4}3m$. The structures of eight crystals (including the isotypic compounds Ce_4RuMg and Ce_4RuCd) have been refined from X-ray single-crystal diffractometer data. The structures are composed of condensed RE_6T trigonal prisms which form a rigid network with adamantane-like topology. Large cavities within these networks are filled with empty RE_6 octahedra and Al_4, In_4, Mg_4, or Cd_4 tetrahedra, respectively. Some of the RE_4TAl and RE_4TIn show small homogeneity ranges that result from small degrees of Al/T and In/T mixing on the 16*e* sites. All cerium compounds show small anomalies in the plots of the cell volumes. This is confirmed by temperature-dependent magnetic susceptibility measurements. Ce_4RuMg, Ce_4RuCd, Ce_4RuAl, and Ce_4RuIn show intermediate cerium valence and no magnetic ordering down to 3 K. Ce_4RhAl shows essentially trivalent cerium.

Keywords Intermetallic compounds · Aluminides · Crystal chemistry

F. Tappe · C. Schwickert · S. Linsinger · R. Pöttgen (✉)
Institut für Anorganische und Analytische Chemie,
Westfälische Wilhelms-Universität Münster,
Corrensstrasse 30, 48149 Münster, Germany
e-mail: pottgen@uni-muenster.de

Introduction

The rare earth-rich parts of the ternary systems *RE*–*T*–*X* (*RE* = rare-earth element, *T* = transition metal, *X* = Mg, Cd, Al, In) all show one common structure type which was first observed for Gd_4RhIn [1]. In this structure, the rhodium atoms have slightly distorted trigonal prismatic gadolinium coordination. These Gd_6Rh prisms are condensed via common corners and edges to a rigid three-dimensional network which leaves large cavities that are filled with empty octahedra of rare-earth atoms and In_4 tetrahedra, a rare structural motif in solid-state structures (Fig. 1). These tetrahedra have also been observed in the series of isotypic RE_4IrIn [2] compounds.

Shortly after the discovery of the RE_4TIn indides, several isotypic series RE_4TMg [3, 4, 5, and references therein] and RE_4TCd [6, 7, and references therein] with different transition metals were synthesized and structurally characterized. Substitution of trivalent indium by divalent magnesium and cadmium, together with a change in the transition-metal component, leads to a change in the valence electron concentration (VEC), and one can thus effectively fine-tune the physical properties of these intermetallics.

Although today more than 160 RE_4TX compounds [3, 4, 5, 6, 7, and references therein] with the cubic Gd_4RhIn-type structure have been synthesized, only a few of them have been characterized with respect to their chemical and physical properties. Besides the variation in VEC through complete substitution, the RE_4TX compounds show diverse examples with extended solid solutions. The X_4 tetrahedra show solid solutions $Mg_{4-x}Al_x$ [8] or $In_{4-x}Mg_x$ [2], and in the case of the RE_4TMg series the rare-earth site shows some degree of magnesium occupancy, i.e., $RE_{4-x}Mg_xT$Mg [9]. The Mg/Al substitution in $Gd_4NiMg_{1-x}Al_x$ [8] has a drastic effect on the magnetic behavior. $Gd_4NiMg_{1-x}Al_x$

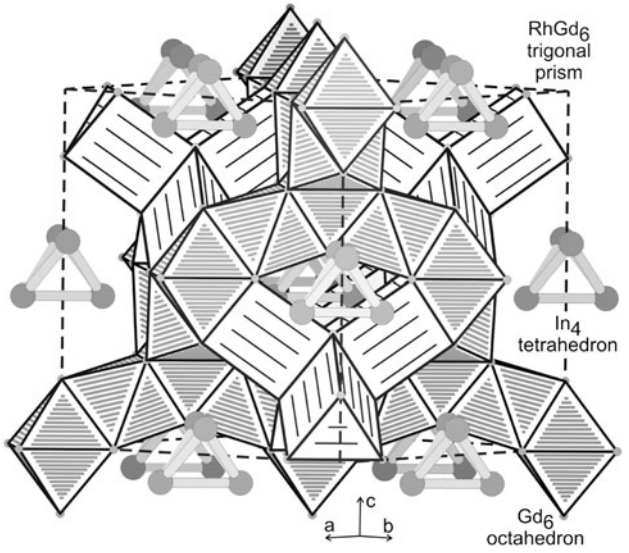

Fig. 1 Crystal structure of Gd_4RhIn. The network of condensed Gd_6Rh trigonal prisms, the empty Gd_6 octahedra, and the In_4 tetrahedra are emphasized

samples show a transition from antiferromagnetic ordering to spin-glass behavior with increasing aluminum content [8]. Another interesting topic concerns the hydrogenation behavior. Gd_4NiMg [9] absorbs up to 11 hydrogen atoms per formula unit, i.e., almost two hydrogen atoms per metal atom of the host structure. One of the highly interesting compounds with potential application is Er_4NiCd [6], which shows a large reversible magnetocaloric effect due to a rather unstable antiferromagnetic ground state and a high relative cooling power (RCP) of 595 J kg^{-1}.

In the course of our systematic studies on phase formation, structure, and physical properties of RE_4TX intermetallics we have now obtained the series of RE_4TAl aluminides. To date, only La_4RuAl and Ce_4RuAl have been reported at a conference [10]. In addition we report on RE_4RuIn indides and a comparison of the structures of Ce_4RuMg, Ce_4RuCd, Ce_4RuAl, and Ce_4RuIn. These phases are of special interest, since cerium–ruthenium intermetallics show a pronounced tendency for intermediate cerium valence accompanied by significantly shortened Ce–Ru distances [11–14, and references therein].

Results and discussion

Structure refinements

In agreement with the powder lattice parameters (Table 1), the eight diffractometer data sets showed face-centered cubic lattices and no further extinctions, in accordance with our previous work on Gd_4RhIn [1], space group $F\bar{4}3m$. The atomic parameters of Gd_4RhIn were then taken as starting

Table 1 Lattice parameters (Guinier powder data) of rare earth-rich compounds with cubic Gd_4RhIn-type structure

Compound	*a*/pm	*V*/nm^3	Reference
RE_4RuMg			
La_4RuMg	1,433.6(2)	2.9463	[3]
Ce_4RuMg	1,408.1(2)	2.7919	[3]
Pr_4RuMg	1,405.9(1)	2.7788	[3]
Nd_4RuMg	1,399.5(3)	2.7411	[3]
RE_4RuAl			
La_4RuAl	1,408.3(2)	2.7931	[10]
Ce_4RuAl	1,377.1(1)	2.6115	[10]
Ce_4RuAl	1,377.4(3)	2.6133	This work
Pr_4RuAl	1,384.3(2)	2.6527	This work
Nd_4RuAl	1,374.5(1)	2.5969	This work
Sm_4RuAl	1,360.9(3)	2.5204	This work
Gd_4RuAl	1,355.9(2)	2.4929	This work
Tb_4RuAl	1,347.0(2)	2.4437	This work
Dy_4RuAl	1,341.3(2)	2.4132	This work
Ho_4RuAl	1,335.1(3)	2.3799	This work
RE_4RuCd			
La_4RuCd	1,415.9(1)	2.8386	[20]
Ce_4RuCd	1,393.4(1)	2.7053	[20]
Pr_4RuCd	1,392.4(1)	2.6994	[20]
Nd_4RuCd	1,388.0(1)	2.6742	[20]
RE_4RuIn			
La_4RuIn	1,424.1(1)	2.8884	This work
Ce_4RuIn	1,396.2(1)	2.7217	[10]
Ce_4RuIn	1,396.3(2)	2.7225	This work
Pr_4RuIn	1,399.9(1)	2.7434	This work
Nd_4RuIn	1,391.1(3)	2.6922	This work
Sm_4RuIn	1,380.9(4)	2.6331	This work
RE_4RhAl			
Y_4RhAl	1,355.0(1)	2.4880	This work
La_4RhAl	1,418.3(3)	2.8528	This work
Ce_4RhAl	1,394.6(3)	2.7124	This work
Pr_4RhAl	1,390.0(1)	2.6855	This work
Nd_4RhAl	1,381.8(1)	2.6386	This work
Sm_4RhAl	1,369.7(1)	2.5697	This work
Gd_4RhAl	1,357.2(1)	2.5001	This work
Tb_4RhAl	1,350.1(2)	2.4611	This work
Dy_4RhAl	1,346.8(2)	2.4430	This work
Ho_4RhAl	1,341.5(2)	2.4143	This work
Er_4RhAl	1,332.3(2)	2.3650	This work
Tm_4RhAl	1,328.9(1)	2.3468	This work
Lu_4RhAl	1,318.0(1)	2.2894	This work
RE_4IrAl			
La_4IrAl	1,417.7(2)	2.8492	This work
Ce_4IrAl	1,395.1(1)	2.7152	This work
Pr_4IrAl	1,394.2(3)	2.7098	This work
Nd_4IrAl	1,385.1(3)	2.6573	This work
Sm_4IrAl	1,369.8(1)	2.5703	This work

Table 1 continued

Compound	*a*/pm	*V*/nm^3	Reference
Gd_4IrAl	1,359.7(1)	2.5135	This work
Tb_4IrAl	1,351.8(1)	2.4703	This work
Dy_4IrAl	1,345.9(2)	2.4383	This work
Ho_4IrAl	1,338.7(1)	2.3992	This work
Er_4IrAl	1,330.5(2)	2.3550	This work
RE_4IrIn			
La_4IrIn	1,437.2(3)	2.9683	This work
Ce_4IrIn	1,413.2(2)	2.8221	This work
Pr_4IrIn	1,404.4(2)	2.7701	This work
Nd_4IrIn	1,399.0(3)	2.7380	This work
Sm_4IrIn	1,385.9(2)	2.6617	This work

The lattice parameters of some isotypic magnesium and cadmium compounds are listed for comparison

values, and the structures were refined using SHELXL-97 [15, 16] (full-matrix least-squares on F^2) with anisotropic atomic displacement parameters for all sites. The occupancy parameters were then refined in a separate series of least-squares cycles. For Ce_4RuMg, Ce_4RuCd, Pr_4IrIn, and Nd_4RuIn all sites were fully occupied within two standard deviations. The remaining four data sets showed too high electron density on the 16*e* site of the *X* component, indicating mixing with the transition metal on this site, similar to the RE_4NiMg series [4]. In the subsequent cycles, these 16*e* sites were refined with mixed occupancy, leading to the compositions listed in Tables 2 and 3. Refinement of the correct absolute structure was ensured through calculation of the Flack parameter [17, 18]. Only the crystals of Ce_4RuMg, Ce_4RuCd, and Nd_4RuIn showed twinning by inversion. The refinements converged to the values listed in Tables 2 and 3. The final difference-Fourier syntheses revealed no significant residues. The highest residuals are a consequence of the high absorption, and such artifacts might accumulate on highly symmetrical sites within a structure refinement. This effect has been discussed in detail in the original work on the series of RE_4RhIn [1] and RE_4IrIn [2] compounds. The refined atomic positions, isotropic displacement parameters, and interatomic distances are given in Tables 4 and 5. Further information on the structure refinements is available (see "Experimental" section).

Crystal chemistry

Thirty-nine new representatives (i.e., aluminides RE_4TAl and indides RE_4TIn) of the cubic Gd_4RhIn-type structure

Table 2 Crystal data and structure refinement for RE_4TX, Gd_4RhIn type, space group $F\bar{4}3m$, $Z = 16$

Empirical formula	Ce_4RuMg	Ce_4RuCd	$Ce_4Ru_{1.27(5)}In_{0.73(5)}$	$Ce_4Rh_{1.14(1)}Al_{0.86(1)}$
Molar mass/g mol^{-1}	685.86	773.95	772.61	701.28
Unit cell dimensions	Table 1	Table 1	Table 1	Table 1
Calculated density/g cm^{-3}	6.53	7.60	7.58	6.87
Crystal size/μm^3	20 × 20 × 40	20 × 20 × 30	10 × 20 × 30	20 × 20 × 40
Detector distance/mm	70	80	60	–
Exposure time/min	8	8	6	–
ω range; increment/deg	0–180; 1.0	0–180; 1.0	0–180; 1.0	–
Integr. param. A, B, EMS	13.0, 3.0, 0.012	12.8, 2.9, 0.012	12.4, 2.9, 0.011	–
Transm. ratio (max/min)	0.264/0.161	0.755/0.504	0.488/0.269	0.562/0.308
Absorption coefficient/mm^{-1}	27.6	31.5	31.2	29.0
F(000), e	4,608	5,184	5,178	4,714
θ range/deg.	2–30	2–30	3–30	2–30
Range in *hkl*	±19, ±19, ±19	±19, ±19, ±19	±19, ±19, ±19	±19, ±19, ±19
Total no. reflections	5,579	7,270	7,261	7,798
Independent reflections/R_{int}	456/0.047	440/0.091	438/0.073	438/0.113
Reflections with $I > 2\sigma(I)/R_\sigma$	435/0.024	378/0.055	367/0.050	379/0.029
Data/parameters	456/20	440/20	438/20	438/20
Goodness of fit on F^2	1.134	0.856	0.831	1.120
*R*1/*wR*2 for $[I > 2\sigma(I)]$	0.028/0.039	0.035/0.025	0.026/0.025	0.023/0.032
*R*1/*wR*2 for all data	0.033/0.040	0.049/0.027	0.041/0.027	0.035/0.035
Extinction coefficient	0.000066(6)	0.000029(3)	0.000018(3)	0.000033(5)
Flack parameter	–	–	0.00(7)	0.00(6)
BASF	0.42(7)	0.27(8)	–	–
Largest diff. peak/hole, e Å^{-3}	2.30/−1.36	2.27/−2.39	5.04/−1.80	4.71/−2.54

Table 3 Crystal data and structure refinement for RE_4TX, Gd_4RhIn type, space group $F\bar{4}3m$, $Z = 16$

Empirical formula	$Ce_4Ir_{1.05(1)}Al_{0.95(1)}$	Pr_4IrIn	Nd_4RuIn	$Gd_4Rh_{1.09(1)}Al_{0.91(1)}$
Molar mass/g mol^{-1}	787.92	870.66	792.85	765.87
Unit cell dimensions	Table 1	Table 1	Table 1	Table 1
Calculated density/g cm^{-3}	7.71	8.35	7.82	8.14
Crystal size/μm^3	10 × 20 × 50	5 × 30 × 30	10 × 20 × 40	10 × 40 × 40
Detector distance/mm	70	70	80	70
Exposure time/min	6	10	6	6
ω range; increment/deg.	0–180; 1.0	0–180; 1.0	0–180; 1.0	0–180; 1.0
Integr. param. A, B, EMS	12.8, 2.9, 0.012	12.7, 2.4, 0.011	12.6, 2.4, 0.012	12.7, 2.8, 0.012
Transm. ratio (max/min)	0.502/0.197	0.867/0.391	0.680/0.373	0.810/0.254
Absorption coefficient/mm^{-1}	46.8	49.9	35.7	44.7
F(000), e	5,203	5,792	5,328	5,071
θ range/deg.	2–30	2–30	2–30	2–30
Range in hkl	±19, ±19, ±19	±19, ±19, ±19	±19, ±19, ±19	±19, ±19, ±19
Total no. reflections	7,315	7,424	7,235	6,862
Independent reflections/R_{int}	440/0.088	451/0.205	438/0.060	420/0.065
Reflections with $I > 2\sigma(I)/R_\sigma$	397/0.042	358/0.112	406/0.033	381/0.034
Data/parameters	440/20	451/18	438/20	420/20
Goodness of fit on F^2	1.039	0.968	0.952	1.062
$R1/wR2$ for $[I > 2\sigma(I)]$	0.034/0.040	0.064/0.058	0.026/0.021	0.031/0.027
$R1/wR2$ for all data	0.042/0.041	0.090/0.063	0.031/0.022	0.038/0.028
Extinction coefficient	0.000072(6)	–	0.000084(3)	0.000039(4)
Flack parameter	0.01(2)	0.00(4)	–	–0.02(4)
BASF	–	–	0.36(4)	–
Largest diff. peak/hole/e Å^{-3}	4.10/−2.63	5.83/−4.54	3.26/−2.08	2.34/−2.34

(Fig. 1) have been synthesized and structurally characterized. The main structural features of the structure type have already been stressed in the "Introduction." For detailed discussion of the crystal chemical peculiarities of the so-called 4-1-1 compounds we refer to previous work [1, 3, 9]. Chemical bonding has exemplarily been investigated on La_4CoMg [19] and La_4RuMg [3]. These studies underlined the strong covalent La–Co and La–Ru bonding within the network of condensed trigonal prisms. Herein, we focus mainly on the structural anomalies observed for the cerium-containing compounds.

In Fig. 2 we present the course of the cell parameters of the RE_4RhAl series. As expected from the lanthanide contraction, the cell volume decreases from the lanthanum to the lutetium compound. The volume of Y_4RhAl fits between Gd_4RhAl and Tb_4RhAl, similar to the RE_4CoMg series [19]. No pronounced anomaly is detected for Ce_4RhAl, in agreement with the magnetic data discussed below. The cell volume smoothly fits in the Iandelli plot. In contrast we observe significant deviations for Ce_4RuMg [3], Ce_4RuCd [20], Ce_4RuAl [10], and Ce_4RuIn [10]. In Fig. 3 we present cut-outs of the respective volume plots, only showing the lanthanum, cerium, praseodymium, and neodymium volumes. The four cerium compounds show negative anomalies which readily point to mixed cerium valence. This anomaly is most pronounced for Ce_4RuAl, whose cell volume is even smaller than that of Nd_4RuAl. These features are addressed again in the following section discussing the magnetic behavior of Ce_4RuMg, Ce_4RuCd, Ce_4RuAl, and Ce_4RuIn.

Finally we return to the ruthenium displacement parameters, which are enhanced for the respective cerium compounds Ce_4RuMg, Ce_4RuCd, and Ce_4RuIn, while those of the T atoms in the other compounds are in the normal range. This is a direct consequence of the intermediate cerium valence. The ruthenium coordinations are strongly influenced by the cerium valences, and thus the effective sizes of the cerium atoms, i.e., larger Ce^{III} and smaller Ce^{IV}. Consequently one observes larger displacement parameters for the ruthenium sites which tend to optimize their Ce–Ru bonding. Similar trends have been observed in the series of $RE_{23}Ru_7Cd_4$ [21] and $RE_{23}Ru_7Mg_4$ [22] compounds, in which only the intermediate valent cerium compounds $Ce_{23}Ru_7Cd_4$ and $Ce_{23}Ru_7Mg_4$ exhibit enhanced ruthenium displacements.

Concerning the interatomic distances, the main influence is observed for the Ce–Ru distances. Since for the RE_4RuMg series most data sets are available, i.e.,

Table 4 Atomic coordinates and isotropic displacement parameters (pm^2) of RE_4TX

Atom	Wyckoff site	x	y	z	U_{eq}
Ce_4RuMg					
Ce1	24*g*	0.43987(7)	3/4	3/4	192(2)
Ce2	24*f*	0.81228(7)	0	0	157(2)
Ce3	16*e*	0.65479(5)	*x*	*x*	164(2)
Ru	16*e*	0.86275(9)	*x*	*x*	401(5)
Mg	16*e*	0.4217(2)	*x*	*x*	121(12)
Ce_4RuCd					
Ce1	24*g*	0.55981(9)	1/4	1/4	162(3)
Ce2	24*f*	0.19016(9)	0	0	145(3)
Ce3	16*e*	0.34766(7)	*x*	*x*	144(3)
Ru	16*e*	0.13660(10)	*x*	*x*	357(6)
Cd	16*e*	0.57798(8)	*x*	*x*	119(4)
$Ce_4Ru_{1.27(5)}In_{0.73(5)}$					
Ce1	24*g*	0.44152(8)	3/4	3/4	151(3)
Ce2	24*f*	0.80834(8)	0	0	137(3)
Ce3	16*e*	0.65199(6)	*x*	*x*	125(3)
Ru1	16*e*	0.86330(9)	*x*	*x*	313(5)
73(5)% In	16*e*	0.42016(7)	*x*	*x*	94(4)
27(5)% Ru2					
$Ce_4Rh_{1.14(1)}Al_{0.86(1)}$					
Ce1	24*g*	0.43756(6)	3/4	3/4	161(2)
Ce2	24*f*	0.80473(7)	0	0	154(2)
Ce3	16*e*	0.64982(5)	*x*	*x*	124(2)
Rh1	16*e*	0.85814(7)	*x*	*x*	173(4)
86(1)% Al	16*e*	0.42185(24)	*x*	*x*	273(18)
14(1)% Rh2					
$Ce_4Ir_{1.05(1)}Al_{0.95(1)}$					
Ce1	24*g*	0.43945(8)	3/4	3/4	161(3)
Ce2	24*f*	0.80407(9)	0	0	143(3)
Ce3	16*e*	0.65079(6)	*x*	*x*	116(3)
Ir1	16*e*	0.85859(5)	*x*	*x*	137(2)
95(1)% Al	16*e*	0.4221(4)	*x*	*x*	284(30)
5(1)% Ir2					
Pr_4IrIn					
Pr1	24*g*	0.44209(19)	3/4	3/4	128(6)
Pr2	24*f*	0.81092(19)	0	0	92(6)
Pr3	16*e*	0.65094(14)	*x*	*x*	85(7)
Ir	16*e*	0.85806(10)	*x*	*x*	85(5)
In	16*e*	0.4192(2)	*x*	*x*	91(9)
Nd_4RuIn					
Nd1	24*g*	0.55866(6)	1/4	1/4	127(2)
Nd2	24*f*	0.19215(6)	0	0	104(2)
Nd3	16*e*	0.34749(4)	*x*	*x*	94(2)
Ru	16*e*	0.13788(6)	*x*	*x*	122(3)
In	16*e*	0.58049(5)	*x*	*x*	97(2)
$Gd_4Rh_{1.09(1)}Al_{0.91(1)}$					
Gd1	24*g*	0.56346(6)	1/4	1/4	107(2)
Gd2	24*f*	0.19270(7)	0	0	98(2)
Gd3	16*e*	0.35128(6)	*x*	*x*	106(2)
Rh1	16*e*	0.14245(9)	*x*	*x*	112(4)
91(1)% Al	16*e*	0.5782(2)	*x*	*x*	144(21)
9(1)% Rh2					

U_{eq} is defined as one-third of the trace of the orthogonalized U_{ij} tensor

Table 5 Interatomic distances (pm) in Ce_4RuMg, calculated with the powder lattice parameters

Ce1:	2	Mg	342.9(5)	Ce3:	3	Ru	294.9(2)
	2	Ce3	357.1(1)		3	Ce1	357.1(1)
	2	Ru	357.3(2)		3	Mg	361.8(2)
	4	Ce2	372.5(1)		3	Ce3	379.2(2)
	4	Ce1	378.1(1)		3	Ce2	379.7(1)
Ce2:	2	Ru	282.4(1)	Ru:	3	Ce2	282.4(1)
	2	Mg	364.5(3)		3	Ce3	294.9(2)
	4	Ce1	372.5(1)		3	Ce1	357.3(2)
	4	Ce2	373.8(1)	Mg:	3	Mg	312(1)
	2	Ce3	379.7(1)		3	Ce1	342.9(5)
					3	Ce3	361.8(2)
					3	Ce2	364.5(1)

Standard deviations are given in parentheses. All distances within the first coordination sphere are listed

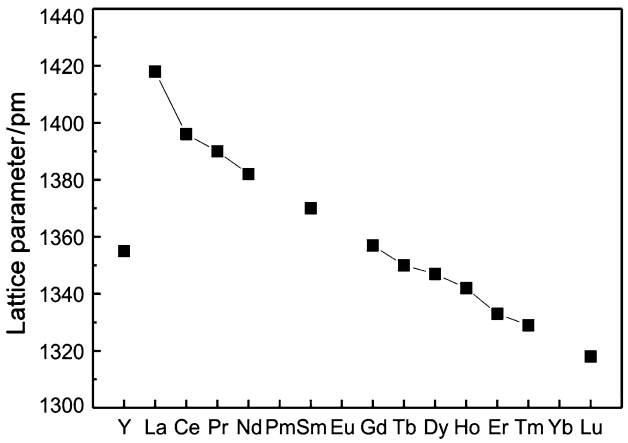

Fig. 2 Course of the cell volumes in the series of RE_4RhAl compounds

Ce_4RuMg reported herein and RE_4RuMg (RE = La, Pr, Nd) in [3], we briefly comment on this behavior. The shortest Ru–*RE* distances are 288 pm in La_4RuMg, 282 pm in Ce_4RuMg, 283 pm in Pr_4RuMg, and 282 pm in Nd_4RuMg. Thus, the intermediate cerium valence leads to slight shrinking of the ruthenium-centered prisms, while the Mg–Mg distances of the Mg_4 tetrahedra are in line with

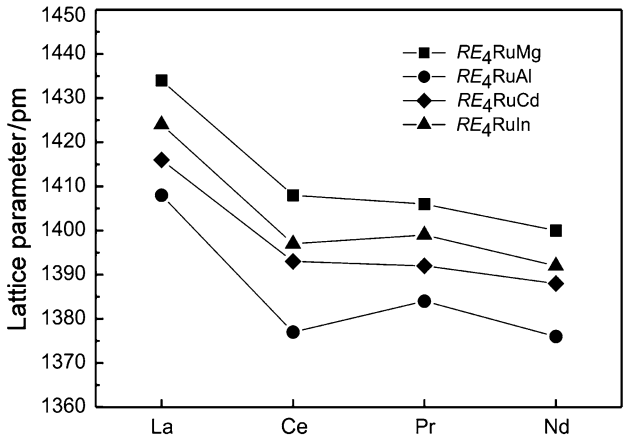

Fig. 3 Course of the cell volumes in the series of RE_4RuX (X = Mg, Al, Cd, In) compounds

the lanthanide contraction. This behavior is expected for all RE_4RuX and $RE_{23}Ru_7X_4$ series.

Magnetic properties

Figure 4 depicts the temperature dependence of the susceptibility and inverse susceptibility (χ and χ^{-1} data) of (a) Ce_4RuMg, (b) Ce_4RuAl, (c) Ce_4RuCd, and (d) Ce_4RuIn. None of the aforementioned compounds show any magnetic ordering down to the lowest measured temperature of 3 K. We were however able to fit the χ^{-1} data of all four compounds using the modified Curie–Weiss law $\chi = \chi_0 + C/(T - \theta)$ in the temperature range 20–300 K. The resulting magnetic data are listed in Table 6. Compound (b) exhibits a magnetic moment of 1.74(1) μ_B/Ce atom. Compounds (a), (c), and (d) show similar magnetic moments of 1.93(1), 1.94(1), and 1.94(1) μ_B/Ce atom, respectively. These magnetic moments are significantly lower than the expected values (2.54 μ_B/Ce^{3+} ion), which can in part be attributed to crystal-field effects as well as splitting of the magnetic ground states at low temperatures, but is primarily due to an intermediate valence state of the

Table 6 Magnetic properties of Ce_4TX (T = Ru, Rh; X = Mg, Al, Cd, In)

Compound	μ_{eff}/μ_B/Ce	θ_P/K	χ_0/emu mol^{-1}	μ_{sm}/μ_B/Ce	% Ce^{3+}
Ce_4RuMg	1.93(1)	−4.0(5)	2.52(1) × 10^{-3}	0.84(1)	58
Ce_4RuAl	1.74(1)	−34.1(5)	3.50(1) × 10^{-3}	0.36(1)	47
Ce_4RuCd	1.94(1)	−4.8(5)	3.0(1) × 10^{-3}	0.89(1)	58
Ce_4RuIn	1.94(1)	−8.1(5)	3.09(1) × 10^{-3}	0.84(1)	58
Ce_4RhAl	2.49(1)	−38.0(5)	–	0.80(1)	100

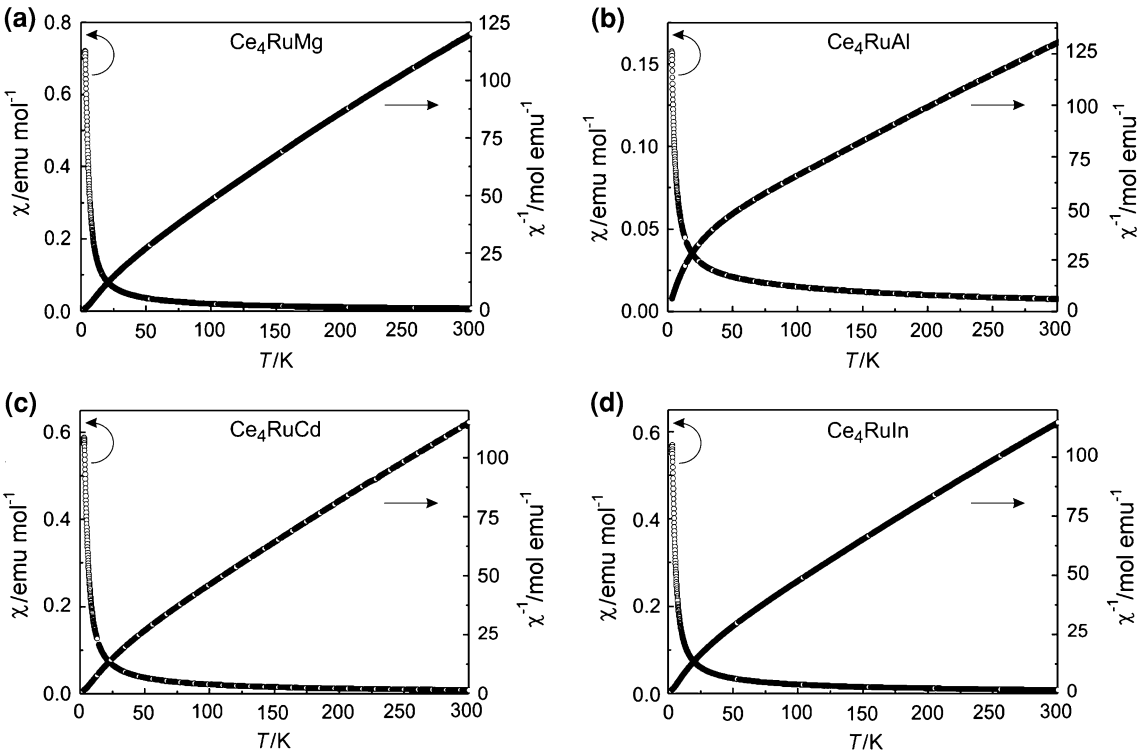

Fig. 4 Temperature dependence of the magnetic susceptibility (χ and χ^{-1} data) of Ce_4RuMg, Ce_4RuCd, Ce_4RuAl, and Ce_4RuIn measured at 10 kOe

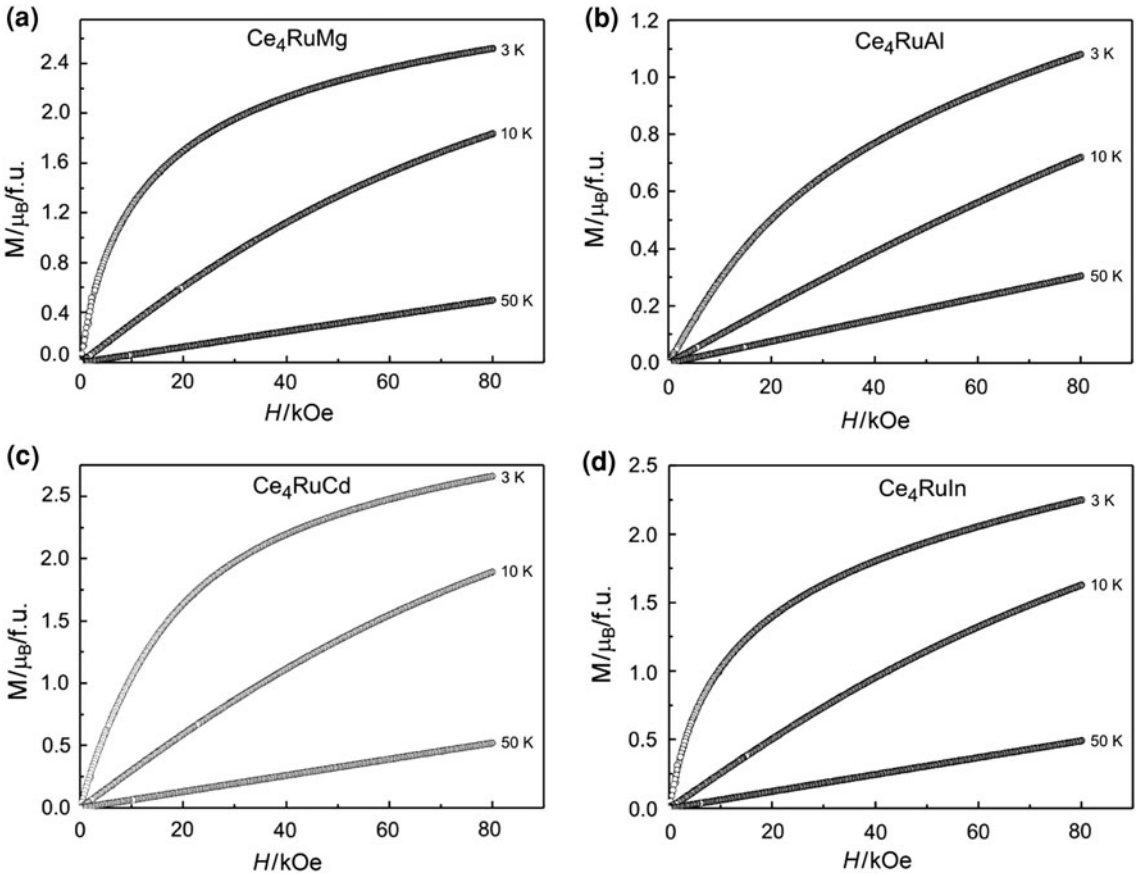

Fig. 5 Magnetization isotherms of Ce_4RuMg, Ce_4RuCd, Ce_4RuAl, and Ce_4RuIn measured at 3, 10, and 50 K

cerium atoms. The negative values of θ_P for all four compounds (Table 6) indicate antiferromagnetic interactions in the paramagnetic region.

The magnetization isotherms of (a) Ce_4RuMg, (b) Ce_4RuAl, (c) Ce_4RuCd, and (d) Ce_4RuIn taken at 3, 10, and 50 K are shown in Fig. 5. Again, an almost linear increase of the magnetization with applied field at 50 K is observed for all four compounds, as expected for paramagnetic materials. At 3 K the curvature of all four magnetization isotherms becomes more pronounced and shows a tendency for saturation at high fields. The isotherms appear to be typical Brillouin functions with field-induced saturation of the paramagnet at low temperatures and high fields. The partial saturation magnetizations μ_{sm} are listed in Table 6, and all of them are significantly smaller than the expected theoretical saturation magnetization $[\mu_{sm}^{\infty}(Ce^{3+}) = 2.14\mu_B]$ according to $g_J \times J$. The susceptibility and magnetization data of the Curie–Weiss paramagnet Ce_4RhAl are presented in Fig. 6 and Table 6. Ce_4RhAl exhibits no magnetic ordering within the investigated temperature range. The experimental effective magnetic moment of 2.49(1) μ_B/Ce atom is in good agreement with the free ion value of 2.54 μ_B for Ce^{3+}.

Experimental

Synthesis

Starting materials for the synthesis of the RE_4TX samples were ingots of the rare-earth metals (Johnson Matthey or Smart Elements), ruthenium, rhodium, and iridium powder (Degussa–Hüls or Heraeus), and an aluminum rod (Chempur) or indium tear drops (Chempur), all with stated purities better than 99.9%. Pieces of the rare-earth ingots were first arc-melted [23] to small buttons under an argon atmosphere of ca. 800 mbar. The argon was purified before with molecular sieves, silica gel, and titanium sponge (900 K). Next the rare-earth buttons, the transition-metal powders, and pieces of aluminum or indium were weighed in 4:1:1 atomic ratio and finally sealed in tantalum tubes under an argon pressure of ca. 800 mbar. The ampoules were placed in a water-cooled sample chamber of a high-frequency furnace (Hüttinger Elektronik, Freiburg, type TIG 1.5/300) under flowing argon [24], first heated at about 1,473 K, and kept at that temperature for about 5 min. The temperature was then lowered to ca. 923 K immediately, and the tubes were annealed for another 3 h. Finally the

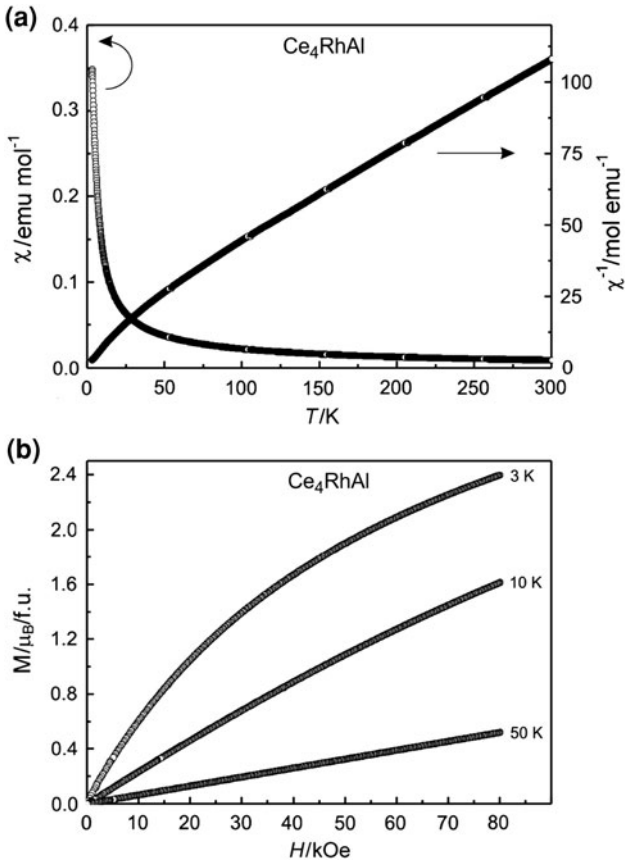

Fig. 6 *Top* temperature dependence of the magnetic susceptibility (χ and χ^{-1} data) of Ce_4RhAl. *Bottom* magnetization isotherms of Ce_4RhAl measured at 3, 10, and 50 K

ampoules were quenched to room temperature. The temperature was controlled through a Sensor Therm Methis MS09 pyrometer with an accuracy of ±30 K. All samples could easily be separated from the ampoules by mechanical fragmentation. No reaction with the container material was observed. The polycrystalline samples were stable in air over weeks.

For crystal growth some of the reactions were carried out in a muffle furnace instead. Therefore, the tantalum tubes were enclosed in evacuated quartz tubes for oxidation protection after sealing. Then the samples were heated to 1,473 K within 4 h and kept at this temperature for another 4 h. Thereafter, the tubes were slowly cooled down to 873 K within 4 days. After another 4 days of annealing at this temperature the furnace was switched off and cooled to room temperature by radiative heat loss. The resulting small single crystals exhibit metallic lustre while the ground powder is dark grey.

Scanning electron microscopy

Some of the bulk samples and the single crystals investigated on the diffractometer were analyzed using a Zeiss EVO® MA10 scanning electron microscope in variable pressure mode with CeO_2, REF_3, Ru, Rh, Ir, Al, and InAs as standards. The bulk samples were previously embedded in a methyl methacrylate matrix, and the surface was polished with diamond and silica paste. The surfaces remained unetched for the energy-dispersive X-ray (EDX) measurements. No impurity elements heavier than sodium were observed. The experimentally determined compositions were close to the ideal ones.

X-ray diffraction data

The polycrystalline RE_4TAl and RE_4TIn samples were studied by powder X ray diffraction using a Guinier camera (image plate system, Fujifilm, BAS-1800, Cu $K_{\alpha 1}$ radiation) and α-quartz ($a = 491.30$, $c = 540.46$ pm) as an internal standard. The cubic lattice parameters (Table 1) were deduced from the powder data using a least-squares routine. The experimental patterns were compared with calculated [25] ones to ensure proper indexing.

Single crystals were selected from the slowly cooled samples by mechanical fragmentation. They were glued to quartz fibers using beeswax and characterized by Laue photographs on a Buerger camera (white molybdenum radiation, image plate technique, Fujifilm, BAS-1800). Data sets of suitable Ce_4RuMg, Ce_4RuCd, Ce_4RuIn, Ce_4IrAl, Pr_4IrIn, Nd_4RuIn, and Gd_4RhAl crystals were collected at room temperature by use of a Stoe IPDS-II image plate system (graphite monochromatized Mo radiation; $\lambda = 71.073$ pm) in oscillation mode. Numerical absorption corrections were applied to the data. The Ce_4RhAl crystal was measured at room temperature by use of a four-circle diffractometer (CAD4) with graphite monochromatized Mo K_α radiation and a scintillation counter with pulse height discrimination. The scans were taken in $\omega/2\theta$ mode, and a numerical absorption correction was applied. All relevant crystallographic data and details of the data collections and evaluations are listed in Tables 2 and 3.

Details may be obtained from Fachinformationszentrum Karlsruhe, D-76344 Eggenstein-Leopoldshafen (Germany) by quoting registry nos. CSD–423265 (Ce_4RuMg), CSD–423264 (Ce_4RuCd), CSD–423261 ($Ce_4Ru_{1.27}In_{0.73}$), CSD–423259 ($Ce_4Rh_{1.14}Al_{0.86}$), CSD–423258 ($Ce_4Ir_{1.05}Al_{0.95}$), CSD–423263 (Pr_4IrIn), CSD–423262 (Nd_4RuIn), and CSD–423260 ($Gd_4Rh_{1.09}Al_{0.91}$).

Magnetic susceptibility measurements

Magnetic measurements were performed in the temperature range of 3–300 K using a Quantum Design physical property measurement system at magnetic flux densities up to 80 kOe. All measurements were carried out using the

VSM option by packing the sample in Kapton foil and attaching it to a brass sample holder.

Acknowledgments We thank Dipl.-Ing. U. Ch. Rodewald for the intensity data collections. This work was financially supported by the Deutsche Forschungsgemeinschaft.

References

1. Zaremba R, Rodewald UC, Hoffmann R-D, Pöttgen R (2007) Monatsh Chem 138:523
2. Zaremba R, Rodewald UC, Hoffmann R-D, Pöttgen R (2008) Monatsh Chem 139:481
3. Tuncel S, Chevalier B, Matar SF, Pöttgen R (2007) Z Anorg Allg Chem 633:2019
4. Rodewald UC, Chevalier B, Pöttgen R (2007) J Solid State Chem 180:1720
5. Solokha P, De Negri S, Pavlyuk V, Saccone A (2009) Chem Met Alloys 2:39
6. Hermes W, Rodewald UC, Pöttgen R (2010) J Appl Phys 108:113919
7. Tappe F, Pöttgen R (2011) Rev Inorg Chem 31:5
8. Linsinger S, Hermes W, Chevalier B, Couillaud S, Bobet J-L, Eul M, Pöttgen R (2009) Intermetallics 17:1028
9. Tuncel S, Roquefère JG, Stan C, Bobet J-L, Chevalier B, Gaudin E, Hoffmann R-D, Rodewald UC, Pöttgen R (2009) J Solid State Chem 182:229
10. Kurenbaeva ZM, Murashova EV, Hannanov DN, Ilyukin AB, Tursina AI, Seropegin YD (2010) XIth international conference on crystal chemistry of intermetallic compounds. Lviv, Ukraine, P61
11. Hermes W, Matar SF, Pöttgen R (2009) Z Naturforsch 64b:901
12. Mishra T, Hoffmann R-D, Schwickert C, Pöttgen R (2011) Z Naturforsch 66b:771
13. Murashova EV, Tursina AI, Bukhanko NG, Nesterenko SN, Kurenbaeva ZM, Seropegin YD, Noël H, Potel M, Roisnel T, Kaczorowski D (2010) Mater Res Bull 45:993
14. Kurenbaeva ZM, Tursina AI, Murashova EV, Nesterenko SN, Seropegin YD (2011) Russ J Inorg Chem 56:218
15. Sheldrick GM (1997) SHELXL-97, Program for crystal structure refinement, University of Göttingen
16. Sheldrick GM (2008) Acta Crystallogr A64:112
17. Flack HD, Bernadinelli G (1999) Acta Crystallogr 55A:908
18. Flack HD, Bernadinelli G (2000) J Appl Crystallogr 33:1143
19. Tuncel S, Hoffmann R-D, Chevalier B, Matar SF, Pöttgen R (2007) Z Anorg Allg Chem 633:151
20. Schappacher FM, Pöttgen R (2008) Monatsh Chem 139:1137
21. Tappe F, Hermes W, Eul M, Pöttgen R (2009) Intermetallics 17:1035
22. Linsinger S, Eul M, Hermes W, Hoffmann R-D, Pöttgen R (2009) Z Naturforsch 64b:1345
23. Pöttgen R, Gulden T, Simon A (1999) GIT Labor Fachzeitschrift 43:133
24. Kußmann D, Hoffmann R-D, Pöttgen R (1998) Z Anorg Allg Chem 624:1727
25. Yvon K, Jeitschko W, Parthé E (1977) J Appl Crystallogr 10:73